Supplementary Materials

Predictive Thermal Safety of Lithium-Ion Batteries through a Unified Kinetic-Thermal Framework

Jiale Huang[1], Yiyang Xia[1], Shijia Xu[1], Ling Li[1], Hongbo Ji[1], Xiaoping Chen[1]*, Jun Xu[2, 3]*

* Correspondence to: Dr. Jun Xu: junxu@udel.edu, Dr. Xiaoping Chen: cxp@nbut.edu.cn

[1]*Zhejiang Provincial International Joint Laboratory of New Energy Vehicle Technology, College of Mechanical and Automotive Engineering, Ningbo University of Technology, Ningbo, China*

[2]*Department of Mechanical Engineering, University of Delaware, Newark, DE 19716, USA*

[3]*Energy Mechanics and Sustainability Laboratory (EMSLab), University of Delaware, Newark, DE 19716, USA*

1. Battery property measurements

1.1 Cycle consistency

As shown in Figure S1, the cycling profiles demonstrate excellent reproducibility with negligible variation across cycles, confirming stable and consistent performance under repeated operation.

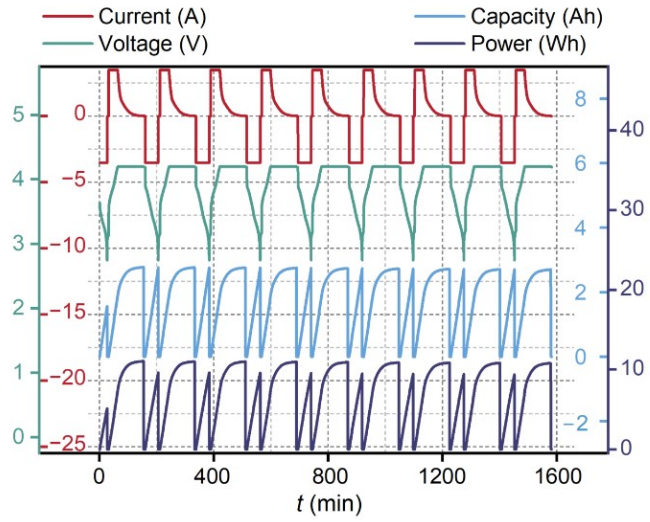

Figure S1. Cycling consistency test for the cell. The insets illustrate the current, voltage, capacity, and power profiles, highlighting the cell's stable performance and minimal degradation across cycles.

1.2 Mass and density test

The mass of the battery cell was measured using an electronic balance. To account for variations among individual cells, 10 randomly selected units were measured, and the average mass was recorded as 4.56×10^{-2} kg. For volume determination, a vernier caliper was used to measure the height and radius of the cell, from which the volume was calculated. Similarly, 10 units were measured to obtain the average value of 1.65×10^{-5} m^3. The density was then calculated

using Eq. (S1) and recorded as 2.76×10^3 kg·m^{-3},

$$\rho = \frac{m}{V} \tag{S1}$$

1.3 Anisotropic thermal conductivity test

The measurement of thermal conductivity in battery cells has attracted substantial research attention, with anisotropy being a key characteristic [S1]. As the present simulations were performed in three dimensions, it was necessary to measure the anisotropic thermal conductivity of the tested unit [S2].

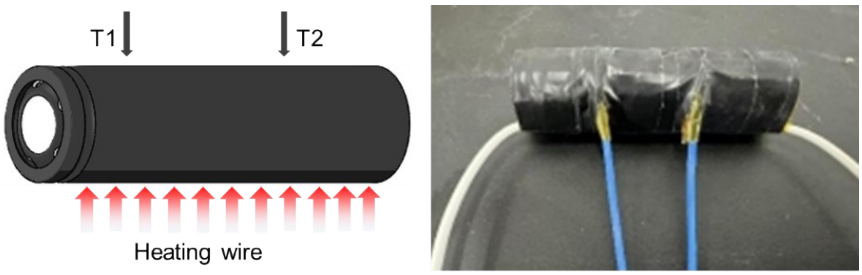

Figure S2. Anisotropic thermal conductivity test. The test setup involved carefully positioned thermocouples to measure temperature gradients and calculate conductivity along both axes.

Drake et al. [S3] analytically solved the corresponding heat transfer governing equations and derived the temperature evolution as a function of time and radial position r, approximately expressed as,

$$\theta(r,t) = \frac{2Q}{\rho c_p R}t + \frac{Q}{k_r R}\left(\frac{r^2}{2} - \frac{R^2}{4}\right) \tag{S2}$$

where θ is the temperature rise, Q is the heating power, c_p is the specific heat, R is the radius of the cylinder, k_r is the radial thermal conductivity. In Eq. (S2) the specific heat capacity (c_p) is obtained from the slope of the fitted line, while the radial thermal conductivity (k_r) is determined

from it intercept. In the experiments, the tested cell, shown in Figure S2, was carefully insulated in sequence with conductive tape, insulating tape, fiberglass, aerogel, and insulating tape to minimize heat loss. The variation of temperature rise with time is presented in Figure S3. From fitted slope and intercept, the results yield $k_r = 0.178 \pm 0.011$ W·m^{-1}·K^{-1} and $c_p = 1008$ J·kg^{-1}·K^{-1}. Using the same method, the axial thermal conductivity was determined as $k_z = 18.12 \pm 1.15$ W·m^{-1}·K^{-1}.

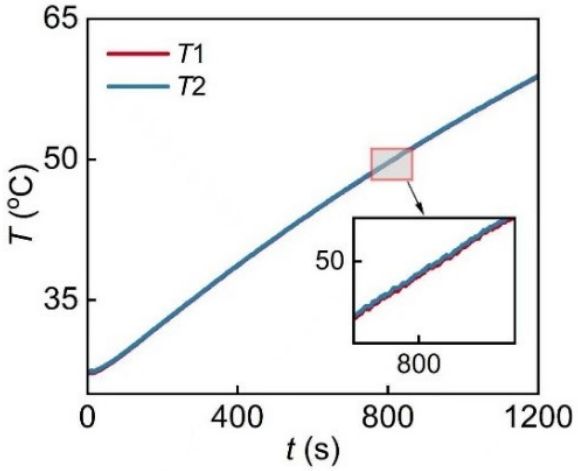

Figure S3. Variation of temperature with time for the thermal conductivity test. The data illustrate the rate of temperature change over time in both radial and axial directions, which is used to determine the cell's thermal properties.

1.4 Specific heat test

It should be noted that, in addition to the method described above, the specific heat capacity can also be measured using accelerating rate calorimetry (ARC) [S4]. Here, a relatively rapid approach was employed to validate the specific heat obtained in the previous experiments. Three cells were bound together in a triangular configuration with conductive tape, and a thermocouple

probe was inserted to contact the wall of each cell. A constant heating power was applied under the ARC thermal insulation environment. By recording the temperature rise over time and extracting the slope of the linear region, the specific heat capacity of the cell can be determined as,

$$c_p = \frac{UI}{m_{total} a_{slope}} \tag{S3}$$

where U is the heating voltage, I is the heating current, m_{total} is the total mass of the cells, a_{slope} is the slope coefficient of the tested linear region. Figure S4 illustrates the temperature rise with time in ARC specific heat test.

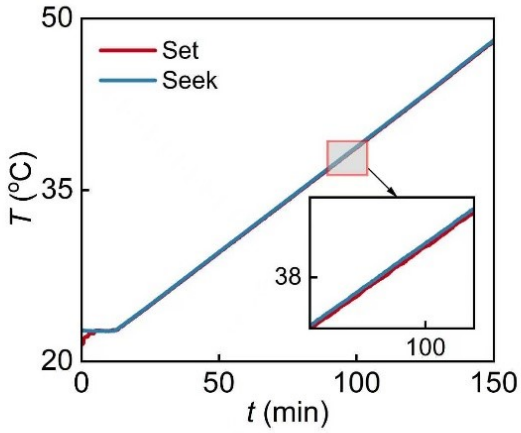

Figure S4. The temperature rises over time in the ARC-specific heat test. The results reveal the relationship between temperature increase and time under controlled heating, which is essential for modeling thermal behavior.

The obtained value of specific heat capacity is 984 $J \cdot kg^{-1} \cdot K^{-1}$. Compared with the result from the previous section (1008 $J \cdot kg^{-1} \cdot K^{-1}$), the deviation is within 2.3%, which is well within the acceptable range for thermal property measurements. Accordingly, a mean value of 996 $J \cdot kg^{-1} \cdot K^{-}$

[1], derived from the two methods, was adopted in the subsequent simulation model.

2. Grid and time-step independence

Ensuring grid and time-step independence is a fundamental prerequisite in numerical simulations, particularly in computational fluid dynamics and heat transfer modelling. The discretization of governing equations inevitably introduces numerical errors, the magnitude of which depends on both the spatial resolution of the computational grid and the temporal resolution of the time step. If the grid is too coarse in this case, the temperature gradients may be under-resolved, leading to inaccurate prediction of key variables. Similarly, if the time step is excessively large, transient dynamics may be distorted or even rendered unstable, compromising the reliability of the simulation. Conversely, refining the grid and reducing the time step beyond necessity increases computational cost without appreciable gain in accuracy. Grid and time-step independence studies therefore serve to identify the balance point where simulation results are no longer sensitive to further refinement.

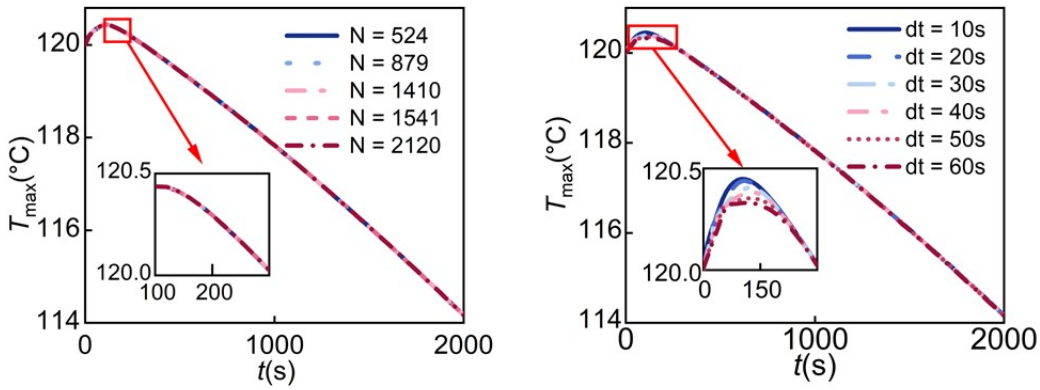

Figure S5. Grid and time step independence check. The analysis confirms that further refinement of the mesh and smaller time steps beyond the selected values do not significantly alter the results.

Figure S5 presents the maximum temperature evolution during cooling of a cell at $h = 5\ W \cdot m^{-2} \cdot K^{-1}$ and 100% SOC, evaluated with varying grid numbers and time steps. Increasing the mesh size from 5240 to 21200 elements produces negligible differences in temperature, indicating that the chosen grid resolution is sufficient. With a fixed mesh size of 14100, deviations emerge when the time step is varied between 10 s and 60 s. Based on these results, a time step of 20 s was selected as the minimum temporal resolution for subsequent simulations.

3. Aspect ratio (*H*/*D*) vs. Surface-to-volume ratio (*S*/*V*)

This section addresses the selection of geometric influencing parameters, specifically aspect ratio and surface-to-volume ratio. For cylindrical batteries, the aspect ratio is defined as the height (H) divided by the radius (D). In broader contexts, such as pouch, prismatic, and blade cells, it refers to the ratio of the longer side length to the shorter side length. Surface-to-volume ratio, with dimensions of m^{-1}, is defined as the total surface area (S) divided by the volume (V). Both parameters significantly affect the thermal behavior of the cell.

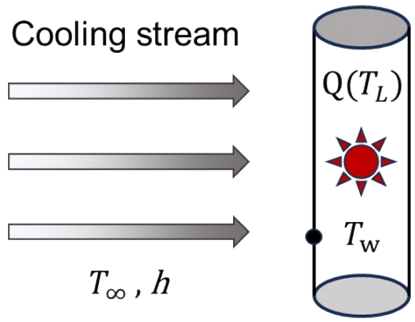

Figure S6. Physical model of transient cooling on a cylinder. The model accounts for convective cooling at the outer surface and internal heat generation with the lumped parameter assumption.

Consider a self-heating cylinder cooled by a stream flow, as illustrated in Figure S6. The

stream temperature is T_∞, and convective heat transfer occurs with coefficient h. The heat generation within the cylinder is temperature-dependent, $Q(T)$, representing the heat generation process of a battery cell, while the wall temperature is T_w. Under the lumped-parameter assumption, the lumped temperature is $T_L = T_w$. Applying energy conservation yields,

$$\rho V c \frac{dT_L}{dt} = -hS(T_L - T_\infty) + Q(T_L) \tag{S4}$$

where ρ is the density, V is the volume, c is the specific heat, S is the surface area. Assuming $Q(T_L)$ in a three-order polynomial form ($aT_L^3 + bT_L^2 + cT_L + d$) and neglecting the lower orders, we can obtain,

$$\frac{1}{2hS} ln \left| \frac{aT_L^2 - hS}{T_L^2} \right| = \frac{t}{\rho V c} + C \tag{S5}$$

Applying the initial boundary condition when $T_L(0) = T_i$ to fix constant C, we obtain,

$$T_L(t) = \sqrt{\frac{hS}{a - \left(a - \frac{hS}{T_i^2}\right) e^{2t\left(\frac{hS}{\rho V c}\right)}}} \tag{S6}$$

The lumped-parameter calculation in Eq. S3 clearly demonstrates that the surface-to-volume ratio directly governs the temperature evolution within the cell. From a heat transfer perspective, the critical safety boundary temperature, the highest initial temperature from which the cell can be cooled without triggering thermal runaway, thus depends primarily on the surface-to-volume ratio rather than the aspect ratio. To further substantiate this viewpoint, comparative studies are conducted as follows.

The aspect ratio of an 18650 cell is 3.61, while its surface-to-volume ratio is 0.253 m^{-1}. By

fixing the aspect ratio and proportionally reducing both the height and radius of the cylinder, the corresponding volume, total surface area, and surface-to-volume ratio can be calculated. The results are summarized in Table S1.

Table S1. Geometric parameters of proportionally reduced cases

H (mm)	D (mm)	V (mm^3)	S (mm^2)	S/V (m^{-1})
65	18	16540.0	4184.5	0.253
60	16.6	13009.1	3565.5	0.274
55	15.2	10020.3	2996.0	0.299
50	13.8	7528.4	2476.0	0.329
45	12.5	5488.2	2005.6	0.365
40	11.1	3854.6	1584.7	0.411
35	9.7	2582.3	1213.3	0.470
30	8.3	1626.1	891.4	0.548
25	6.9	941.1	619.0	0.658
20	5.5	481.8	396.2	0.822

The same simulation method was applied to determine the critical temperature for thermal safety in each case. The heat generation power was proportionally scaled to maintain an identical volumetric heat generation rate across cases. All simulations were performed under conditions of h = 1 W·m^{-2}·K^{-1} and SOC = 100%.

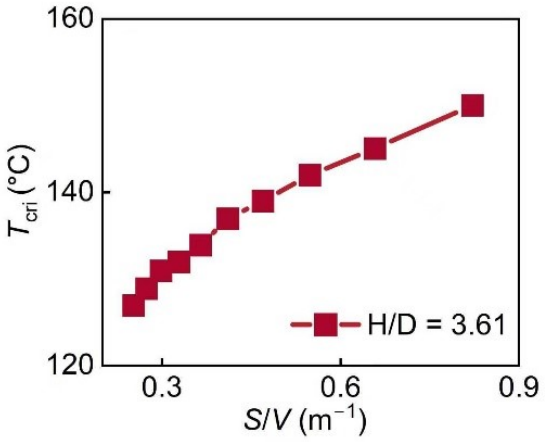

Figure S7. Critical temperature variation with surface-to-volume at fixed aspect ratio. The insets show as S/V increases, the cell's ability to dissipate heat improves, leading to a higher critical temperature and better thermal stability.

Figure S7 shows that the surface-to-volume ratio (S/V) has a pronounced effect on the critical temperature at fixed H/D. As S/V increases from 0.253 to 0.822, the critical temperature rises from 127℃ to 150 ℃. This result further supports our hypothesis that the surface-to-volume ratio is more directly correlated with thermal safety boundaries, providing strong evidence for prioritizing it over aspect ratio in subsequent analysis and discussion.

4. Training by random forest algorithm

Because the number of experimental trials and simulation cases is constrained by limited manpower and computational resources, a predictive approach is required to extend the available results and delineate the full thermal safety boundary. Machine learning has shown strong capability in regression and predictive modelling [S5]. Among various methods, the random forest algorithm was selected in this work due to its robustness against overfitting, effectiveness in handling nonlinear relationships, and ability to deliver reliable predictions even with relatively limited datasets [S6].

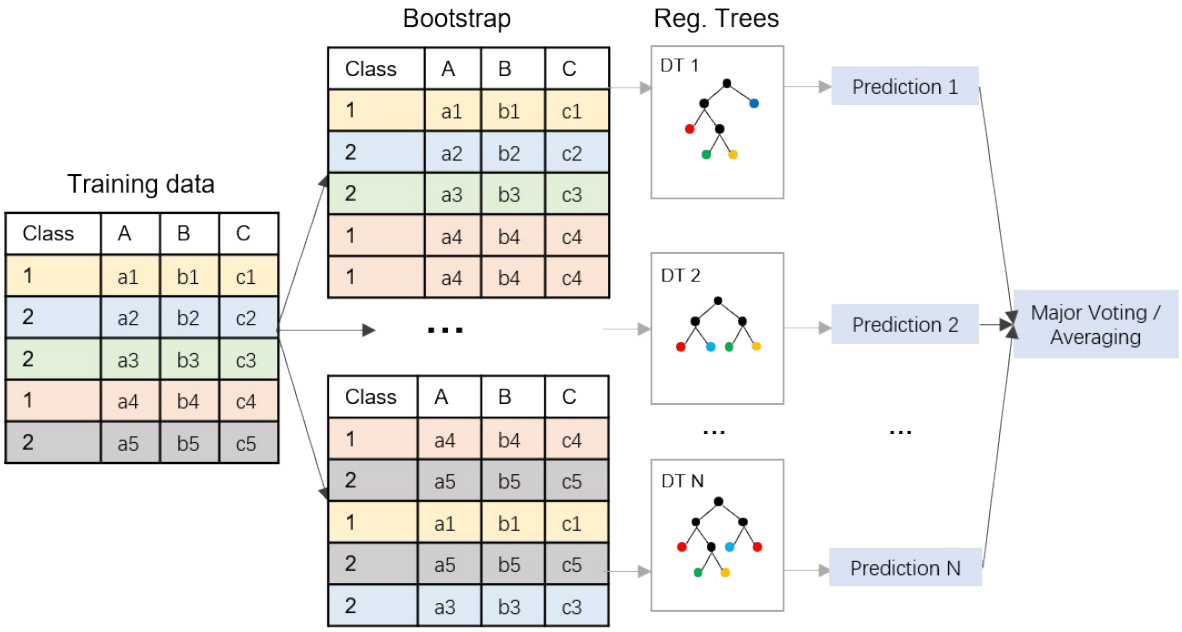

Figure S8. Schematic diagram of the random forest method. Multiple decision trees are trained on experimental and simulated data, and their predictions are aggregated to form a robust model for thermal safety.

Figure S8 illustrates the basic principle of the random forest algorithm. The original dataset is repeatedly resampled to generate multiple bootstrap subsets, each of which is used to train an individual decision tree. Within each tree, predictions are made based on the structure learned from its respective subset. Because each tree is trained on different data, its outputs vary, reflecting the diversity introduced by resampling. The final prediction is obtained by aggregating the outputs of all trees, through majority voting in classification tasks or averaging in regression tasks, thereby reducing variance and improving robustness relative to a single decision tree.

In this work, 135 datasets representing the critical temperature were generated through numerical modelling, of which 103 were used for training and 32 for testing. Regression was

implemented in MATLAB, yielding a mean absolute percentage error (MAPE) of 4.21%. Figure S9 compares the critical temperature from simulation and prediction. This regression approach mitigates data sparsity and enables construction of the thermal safety boundary landscape.

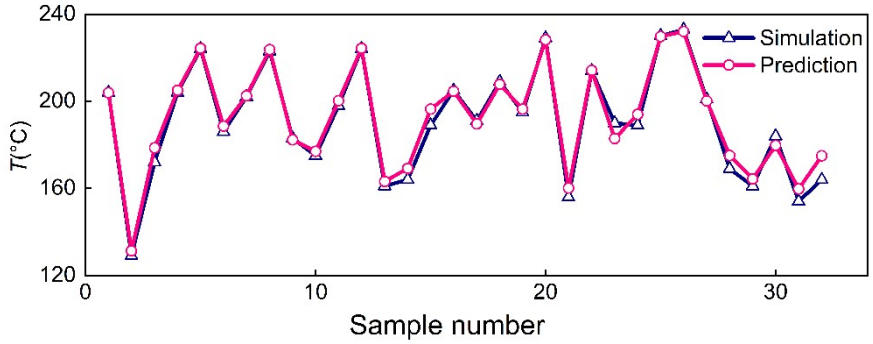

Figure S9. Simulation and comparison of tested samples. The comparison shows a high degree of accuracy, confirming the reliability of the model in predicting thermal runaway behavior across different conditions.

5. Experimental validations

This section employs experimental evidence of thermal safety temperature to validate the simulation results. A heat-stop-cool protocol was applied, in which the tested cell was heated by an electric heating wire bound to the cell wall with a nominal power of 20 W, while simultaneously cooled by an air stream at a controlled velocity.

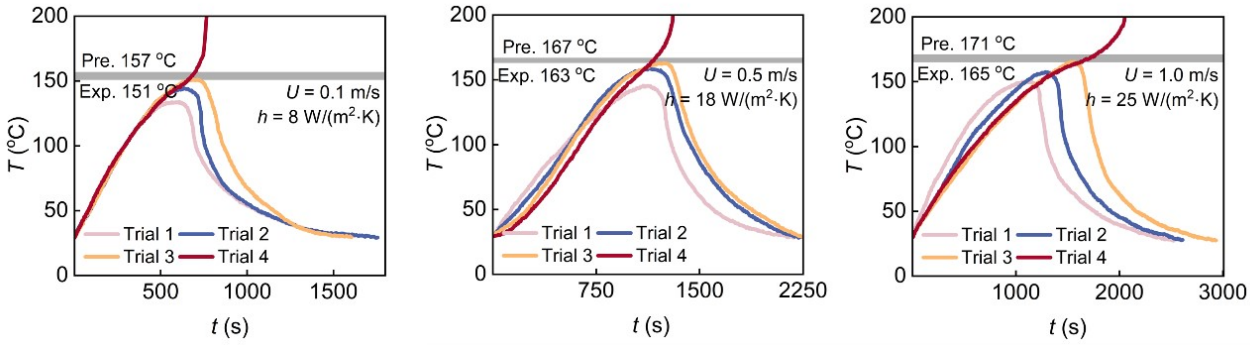

Figure S10. Experimental validation with different cooling stream velocities. The results are used to validate the simulation results and demonstrate how increased cooling stream velocity improves thermal stability and raises the maximum safe operating temperature.

Figure S10 presents the experimental validation process at cooling stream velocities of 0.1, 0.5, and 1.0 m/s, corresponding to average heat transfer coefficients of 8, 18, and 25 $W \cdot m^{-2} \cdot K^{-1}$, respectively. For each case, the trained model predicted critical temperatures of 157 ℃, 167 ℃, and 171 ℃. In the heat-stop-cool experiments, thermal runaway occurred after four successive trials, with the maximum temperatures in the final stable trials recorded as 151 ℃, 163 ℃, and 165 ℃, respectively.

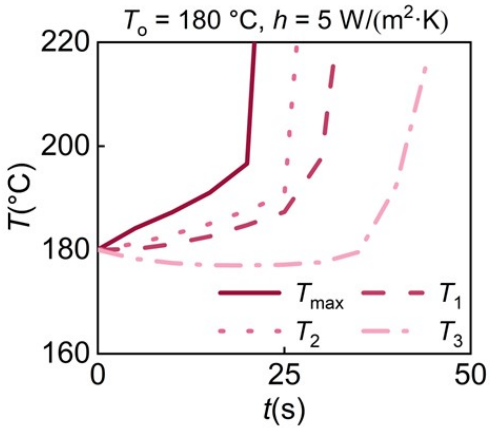

Figure S11. Temperature evolutions at different positions on the cell. The data highlight the temperature gradient between the core and surface, which is crucial for understanding the thermal behavior and runaway onset in cylindrical cells.

It should be noted that a discrepancy exists between the experimentally validated thermal safety temperature and the critical temperature predicted by simulation. One key source of this deviation, as discussed in the main text, is the difference between the maximum internal

temperature of the cell and the temperature measured at the outer wall. Figure S11 illustrates this phenomenon in a representative simulation case. At an initial temperature of 180 ℃ and a convective heat transfer coefficient of 5 $W \cdot m^{-2} \cdot K^{-1}$, a noticeable lag is observed between the wall temperature and the internal peak temperature. Before the onset of thermal runaway, this temperature gradient is substantial and largely unavoidable, leading to an offset between numerical simulation and experimental observation.

References

[1] M. Steinhardt, J. V. Barreras, H. Ruan, B. Wu, G. J. Offer, A. Jossen, Meta-analysis of experimental results for heat capacity and thermal conductivity in lithium-ion batteries: A critical review, Journal of Power Sources 522 (2022) 230829. https://doi.org/10.1016/j.jpowsour.2021.230829

[2] Y. Jiang, J. Huang, P. Xu, P. Wang, Axial and radial thermal conductivity measurement of 18650 lithium-ion battery, Journal of Energy Storage 72 (2023) 108516. https://doi.org/10.1016/j.est.2023.108516

[3] S. J. Drake, D. A. Wetz, J. K. Ostanek, S. P. Miller, J. M. Heinzel, A. Jain, Measurement of anisotropic thermophysical properties of cylindrical Li-ion cells, Journal of Power Sources 252 (2014) 298-304. https://doi.org/10.1016/j.jpowsour.2013.11.107

[4] M. Faber, O. Buitkamp, S. Ritz, M. Börner, J. Berger, J. Friedrich, A. Arzberger, D. U. Sauer, A method to determine the specific heat capacity of lithium-ion battery cells using thermal insulation, Journal of Power Sources 583 (2023) 233499. https://doi.org/10.1016/j.jpowsour.2023.233499

[5] Z. Wei, Q. He, Y. Zhao. Machine learning for battery research, Journal of Power Sources 549 (2022) 232125. https://doi.org/10.1016/j.jpowsour.2022.232125

[6] A. Verikas, A. Gelzinis, M. Macauskiene, Mining data with random forests: A survey and results of new tests, Pattern Recognition 44 (2011) 330-349. https://doi.org/10.1016/j.patcog.2010.08.011